PCCP

RSC Publishing

Interaction of gold nanoparticles with thermoresponsive microgels: influence of the cross-linker density on optical properties†

Kornelia Gawlitza,[a] Sarah T. Turner,[a] Frank Polzer,[b] Stefan Wellert,[a] Matthias Karg,*[c] Paul Mulvaney[d] and Regine von Klitzing*[a]

The interaction of spherical gold nanoparticles (Au-NPs) with microgels composed of chemically cross-linked poly-(*N*-isopropylacrylamide) is reported. Simple mixing of the two components leads to adsorption of the gold particles onto the microgels. Different loading densities can be achieved by varying the ratio of gold particles to microgel particles. The adsorption of gold nanoparticles is analysed by TEM, UV-Vis absorption spectroscopy and SAXS. The influence of the microgel mesh size on the adsorption of gold nanoparticles is investigated by using microgels with three different cross-linker densities. The results suggest a strong relationship between the nanoparticle penetration depth and the cross-linker density. This, in turn, directly influences the optical properties of the colloids due to plasmon resonance coupling. In addition, information about the mesh size distribution of the microgels is obtained. For the first time the change in optical properties by varying cross-linker density and temperature is directly related to the formation of dimers of gold particles, proven by SAXS.

1 Introduction

Microgels are colloidal polymer particles of submicron dimensions with an internal gel-like structure. Microgels based on poly-*N*-isopropylacrylamide (p-NIPAM) can respond to stimuli such as temperature,[1–5] pH[6–8] and ionic strength.[9,10] Hybrid materials can be prepared by combining such microgels with inorganic nanoparticles to create multifunctional particles.[11–14] Ideally these hybrid materials combine the responsiveness of the microgel with the optical, catalytic or magnetic properties of the embedded inorganic material. Many hybrid materials are based on the polymer coating of preformed nanoparticles[15–17] or the *in situ* synthesis of inorganic nanoparticles within a polymer matrix.[18–20] In both cases the nanoparticles are larger than the mesh size and are immobilized within the gel matrix. In the study by Lange *et al.* it was demonstrated that plasmon resonance coupling of Au-NPs can be induced by the contraction of a thermoresponsive p-NIPAM matrix. Simulations show that the plasmon coupling becomes more pronounced, if the distance between the nanoparticle surfaces is below 5 nm.[20] However, to date, only a few studies have dealt with the loading of microgels with preformed nanoparticles. Lyon *et al.* loaded microgel particles with Au-NPs in order to prepare hybrid materials for photothermal patterning of colloidal crystals[21] and for light induced microlens formation.[22] It was demonstrated that strong illumination of a small region of a concentrated sample leads to photothermal crystallisation. However, neither the internal structure of the Au-NP loaded microgels nor any plasmon coupling effects during the volume phase transition of the Au-NPs were investigated. Kumacheva *et al.* attached gold nanorods to copolymer microgels[23] and showed that laser excitation of the longitudinal plasmon resonance of the gold nanorods can be used to induce a collapse of the microgel core. However, the optical properties of the hybrid particles during the volume phase transition were not discussed. Using an approach similar to that of Kumacheva *et al.*, polyelectrolyte-coated gold nanorods were attached at the surface of oppositely charged microgels by Karg *et al.*[24,25] and the optical properties of the gold nanorods were studied as a function of microgel swelling. The microgel collapse led to a significant decrease in the surface area, thereby reducing the distance between the attached gold nanorods. Plasmon coupling was observed below a certain nanorod spacing and the longitudinal plasmon resonance was found to be significantly redshifted.
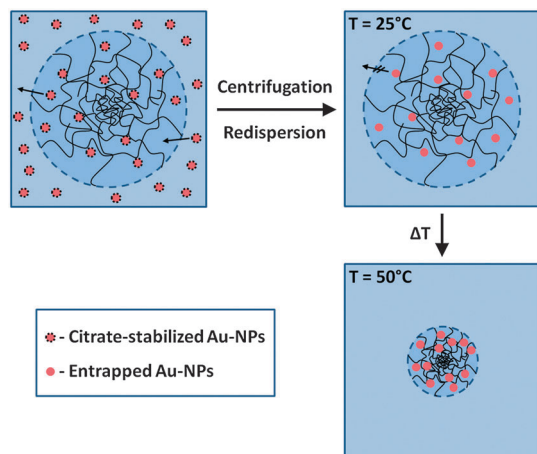
[a] *Technical University of Berlin, Stranski-Laboratory for Physical and Theoretical Chemistry, Institute of Chemistry, 10623 Berlin, Germany. E-mail: klitzing@chem.tu-berlin.de*

[b] *Humboldt University Berlin, Institute of Physics, TEM Group, 12489 Berlin, Germany*

[c] *University of Bayreuth, Physical Chemistry, 95440 Bayreuth, Germany. E-mail: matthias.karg@uni-bayreuth.de*

[d] *University of Melbourne, Bio21 Institute & School of Chemistry, Parkville, Victoria, 3010, Australia*

† Electronic supplementary information (ESI) available. See DOI: 10.1039/c3cp51578h

This journal is © the Owner Societies 2013

Phys. Chem. Chem. Phys., 2013, **15**, 15623–15631 | **15623**

Fig. 1 Scheme of the adsorption process of gold nanoparticles by microgel particles.

In the present paper, the plasmon coupling induced by increase in temperature, Au-NPs concentration and/or cross-linker density is directly related to the formation of dimers of Au-NPs. In addition, the Au-NP distribution is used to monitor the local polymer density within the microgel particles. Citrate stabilised, spherical gold nanoparticles are physically entrapped in chemically cross-linked p-NIPAM microgels, as shown in Fig. 1. UV-Vis absorption spectroscopy is used to monitor changes in the surface plasmon resonance of the Au-NPs upon loading into the microgels. Depending on the loading density, plasmon resonance coupling is observed. This coupling is also strongly dependent on the degree of cross-linking as well as the swelling state of the microgels. Transmission electron microscopy (TEM) is used to study the penetration depth of the Au-NP and dynamic light scattering (DLS) is used to investigate the swelling behaviour of the hybrid particles. Structural changes in the microgel samples are also followed by temperature-dependent SAXS measurements. Here, the high contrast between the Au-NPs and the polymer–water-matrix is beneficial.

2 Experimental methods

2.1 Materials

N-Isopropylacrylamide (97%) (NIPAM) was purchased from Sigma-Aldrich (Munich, Germany). N,N'-Methylenebis(acrylamide) (MBA) ($\geq 99.5\%$), potassium peroxodisulfate (KPS) ($\geq 99\%$), gold(III) chloride hydrate (HAuCl$_4$, $\geq 49\%$) and sodium citrate dihydrate (>99%) were from Fluka (Munich, Germany). NIPAM was purified by recrystallisation in n-hexane and all other chemicals were used as received. A three-stage Millipore Milli-Q Plus 185 purification system was used for water purification.

2.2 Preparation techniques

2.2.1 Synthesis of p-NIPAM microgel particles. Microgel particles with cross-linker concentrations of 0.25 mol% (p-NIPAM$_{0.25}$), 5 mol% (p-NIPAM$_5$) and 10 mol% (p-NIPAM$_{10}$) were synthesised by surfactant-free precipitation polymerisation

according to the protocol reported by Pelton and Chibante.[26] Briefly, 1.132 g of the monomer NIPAM (0.01 mol) and the desired amount of the crosslinker MBA were dissolved in 100 mL of water in a three-neck flask. The temperature of the solution was increased to 70 °C and degassed for 30 min. Afterwards, 1 mL of an aqueous solution of KPS (0.08 M) was added to the mixture while stirring continuously. After 4 h of reaction time the temperature was decreased to room temperature and the mixture was stirred overnight under an N$_2$-atmosphere. The crude microgel particles were purified by filtering over glass wool, dialysing for 2 weeks with daily water exchange and finally freeze drying the particles at −85 °C and 1×10^{-3} bar for 48 h.

2.2.2 Synthesis of gold nanoparticles. Gold nanoparticles (Au-NPs) were synthesised using the well known method of Enüstün and Turkevich.[27] All glassware involved in the synthesis was carefully cleaned with aqua regia. Briefly, 5 mL of a hot citrate solution (0.6 wt%) were added to 100 mL of a boiling gold salt solution (5×10^{-4} M HAuCl$_4$) under vigorous stirring. The growth of the Au-NPs was continued for 17 min leading to a deep red dispersion. Finally, the solution was cooled down to room temperature with continuous stirring.

2.2.3 Loading p-NIPAM microgel particles with Au-NPs. The incorporation of the Au-NPs into the microgels was achieved by adding 0.943 mL of the Au-NPs to 0.057 mL of p-NIPAM microgel solution, resulting in a concentration of 1.9×10^{15} Au-NPs per litre. The concentration of the microgel particles was adjusted to yield Au-NP loadings of either 241 or 1133 Au-NPs per microgel particle. This mixture was homogenised for 10 min using a vortex mixer and then centrifuged at 8000 rpm for 4 min. The residue obtained was then redispersed in 1 mL water. This washing procedure was repeated two times.

2.3 Characterisation methods

2.3.1 Light scattering. The swelling behaviour of the pure microgel particles and the Au-NP loaded microgels was investigated via DLS. The correlation functions were recorded at a constant scattering angle of 60° using an ALV goniometer setup with a HeNe laser as the light source ($\lambda = 632.8$ nm, 35 mW). The correlation functions were generated with an ALV/LSE-5004 correlator followed by analysis using inverse Laplace transformation (CONTIN[28]). The measurements were carried out over a temperature range from 15 °C to 50 °C using a thermostated toluene bath. In addition, DLS measurements at 15 °C and 50 °C were done at angles from 30° to 60° with 15° in between.

Static Light Scattering (SLS) data were recorded at scattering angles from 17° to 37° in 2° steps using an ALV/CGS-3 compact goniometer system equipped with an ALV/LSE-5004 correlator to determine the molecular weight of the polymer particles. The concentration of the polymer particles was varied from 1×10^{-6} g g^{-1} to 7×10^{-6} g g^{-1}. The measurements were recorded at 25 °C using a Huber Compatible Control thermostat. A He–Ne laser ($\lambda = 632.8$ nm, 35 mW) was used and the laser light was polarised vertically with respect to the instrument table.

Zeta potential measurements were carried out with a Malvern Zetasizer NanoZS ($\lambda = 633$ nm, 4 mW) using highly diluted,

15624 | *Phys. Chem. Chem. Phys.*, 2013, **15**, 15623–15631

This journal is © the Owner Societies 2013

aqueous microgel dispersions and the as-synthesized gold nanoparticle dispersion. The temperature during the measurements was 25 °C.

2.3.2 UV-Vis spectroscopy. UV-Vis spectra were collected using a Perkin Elmer Lambda 35 UV-Vis spectrophotometer at a temperature of 25 °C. To obtain temperature dependent UV-Vis spectra in a range from 20 °C to 50 °C a Cary 50 spectrophotometer was used. All spectra were recorded in standard 10 mm quartz cells (Hellma, Germany).

2.3.3 Transmission electron microscopy. TEM specimens were prepared using 5 µL of solution (see preparation techniques for concentrations used) on a TEM copper grid with carbon support film (200 mesh, Science Services, Munich, Germany). The carbon coated copper grids were pretreated using 10 seconds of a glow discharge. The excess of liquid was blotted with a filter paper after 2 minutes. The remaining liquid film on the TEM grid was dried at room temperature for at least one hour. The specimen was inserted into the sample holder (EM21010, JEOL GmbH, Eching, Germany) and transferred to a JEOL JEM 2100 (JEOL GmbH, Eching, Germany). The TEM was operated at an acceleration voltage of 200 kV. All images were recorded digitally using a bottom-mounted 4k × 4k CMOS camera system (TemCam-F416, TVIPS, Gauting, Germany) and processed with a digital imaging processing system (EM-Menu4.0, TVIPS, Gauting, Germany). The final image analysis was completed using ImageJ 1.42q. The number of adsorbed gold nanoparticles was determined by counting the nanoparticles in ten individual microgel particles.

Cryo-TEM specimens were vitrified by plunging the samples into liquid ethane using an automated plunge freezer (Vitrobot Mark IV, FEI Deutschland GmbH, Frankfurt a. M., Germany). The lacey carbon grids were pretreated for 10 seconds with glow discharge. 5 µL of the sample solution was pipetted onto a TEM copper grid with lacey carbon support film (200 mesh, Science Services, Munich, Germany). The liquid was blotted with a filter paper 30 seconds after application of the solution using a 0 blot force for 1 second. No waiting or drain times were used. After vitrification the specimen was inserted into a pre-cooled high-tilt cryo transfer sample holder (Gatan 914, Gatan, Eching, Germany) and transferred into a JEOL JEM 2100 (JEOL GmbH, Eching, Germany). The TEM conditions remained the same as above.

2.3.4 Small angle X-ray scattering (SAXS). SAXS measurements were carried out using a SAXSess mc² system (Anton Paar KG, Graz, Austria). The system is equipped with a sealed tube microsource operated at 40 kV and 50 mA generating Cu-K$_\alpha$ radiation having a wavelength of 0.154 nm. The instrument was aligned in line-collimation operational mode. For the initial data treatment the Saxsquant 3.5 software package was used. Desmearing was carried out by including the measured beam length profile in the desmearing procedure. Data were corrected for dark current and scattering from the blank cell. The samples were measured in a 1 mm quartz capillary and equilibrated for 15 min at 20 °C and 50 °C. The SASfit software (by J. Kohlbrecher from the Paul Scherrer Institute, Villigen, Switzerland) was used for data fitting.

3 Results

3.1 Characterisation of p-NIPAM microgel particles

Three p-NIPAM microgel systems with nominal cross-linker concentrations of 0.25, 5 and 10 mol% were prepared by surfactant-free, precipitation polymerisation. For the sake of clarity, the samples are denoted p-NIPAM$_x$ where x describes the mol% of MBA. The hydrodynamic radii (R_H) were measured by DLS and results for 25 °C and 50 °C are presented in Table 1. The detailed swelling behaviour of the thermoresponsive microgels will be presented in the Discussion section. The hydrodynamic radii of the microgels have to be compared at 50 °C where they are fully collapsed, as during polymerization. Interestingly, the hydrodynamic dimensions of the microgel system with the lowest cross-linker density (p-NIPAM$_{0.25}$) are significantly smaller than those of the p-NIPAM$_5$ and p-NIPAM$_{10}$ particles. This is attributed to less efficient polymerization when a very low concentration of the cross-linker is present.

The swelling behaviour of the microgel particles is controlled by the connectivity of the polymer and may be characterised by the deswelling ratio α, as shown in eqn (1).

$$\alpha = \frac{V_H}{V_{H,0}} = \frac{R_H^3}{R_{H,0}^3} \qquad (1)$$

Here R_H^3 and $R_{H,0}^3$ are the hydrodynamic radii in the collapsed and swollen state, respectively. In our case the hydrodynamic radii at 50 °C and 15 °C were used to calculate the deswelling ratios. The values of α increase linearly with increasing MBA content as shown in Table 1. Due to the higher connectivity in the polymer network at higher MBA concentrations, the microgel particles become less elastic and therefore the deswelling ratio increases. This behaviour of p-NIPAM microgel particles has been intensively studied by, *e.g.* Kratz *et al.*[29,30] The molecular weight of the p-NIPAM microgels was determined using SLS and Zimm-plot analysis. A residual water content of around 10%, which was determined by Karl–Fischer-titration, and a refractive index increment dn/dc = 0.167 cm^{-3} g^{-1} were used in the calculations.[31] The Zimm-plots can be found in the ESI† (Fig. S1). Table 1 summarises the molecular weights of the three microgels. As expected, the lowest molecular weight is found for p-NIPAM$_{0.25}$ (1.7 × 10^9 g mol^{-1}), whereas the values for p-NIPAM$_5$ and p-NIPAM$_{10}$ are somewhat higher, in good agreement with the R_H values.

Zeta potential measurements were performed at 25 °C in order to estimate the p-NIPAM surface charge density. Small, negative values of −7 ± 1 mV were measured for all three microgels (see Table 1). This negative charge is due to the

Table 1 Hydrodynamic radii at 25 °C and 50 °C, deswelling ratios, molecular weights and zeta potentials of p-NIPAM microgel particles with MBA-contents of 0.25, 5 and 10 mol%

MBA [%]	$R_{H,25°C}$ [nm]	$R_{H,50°C}$ [nm]	α	M_W [g mol^{-1}]	ζ [mV]
0.25	239 ± 11	112 ± 5	0.07	1.7 × 10^9 ± 7 × 10^7	−6.5 ± 0.5
5	281 ± 33	169 ± 1	0.15	8.4 × 10^9 ± 3 × 10^8	−5.7 ± 0.5
10	249 ± 10	173 ± 6	0.25	6.9 × 10^9 ± 1 × 10^8	−7.9 ± 0.9

anionic radical initiator used for the polymerisation. Note, that zeta potential values are rather difficult to interpret for large, gel-like particles such as p-NIPAM microgels and therefore ζ serves only as an indication of the slightly negative microgel surface charge.

3.2 Characterisation of Au-NPs

The Au-NPs were characterised using TEM, UV-Vis spectroscopy and SAXS. Fig. 2a shows a representative TEM image of the nearly spherical particles. Fig. 2b shows the size distribution of the Au-NPs with an average radius of 10.3 ± 4.0 nm obtained from measuring the size of at least 100 individual particles from different TEM images. A UV-Vis spectrum recorded from aqueous dispersion at 25 °C is presented in Fig. 2c. The spectrum shows the typical localised surface plasmon resonance leading to an absorption maximum at ≈ 525 nm. Using the optical density of gold the number concentration of Au-NPs could be calculated (2×10^{15} particles per L).

The zeta potential of the citrate stabilised Au-NPs was measured from dilute aqueous dispersion at 25 °C and yielded a surface potential of -30 ± 2 mV.

In addition, the particle size, size distribution and the shape of the pure Au-NPs were all determined by SAXS measurements performed at 20 °C. The obtained scattering profile could be successfully fitted using a form factor for polydisperse spheres, resulting in a particle radius of 12.8 ± 2.4 nm. Since the measurements were performed in the highly dilute regime, any structure factor contribution could be neglected ($S(Q) \approx 1$). The obtained radius is in reasonable agreement with the average radius obtained from TEM, taking the standard deviation into account. The corresponding scattering curve is shown in the ESI† (Fig. S2).

3.3 Loading p-NIPAM microgel particles with Au-NPs

Two different concentrations of Au-NPs were used to load the p-NIPAM microgel particles. The molecular weight of the

microgels (Table 1) allows calculation of the number density of microgel particles in the dispersion. At the same time the number concentration of the Au-NPs dispersion can be calculated using the extinction cross-section of gold. Therefore, the theoretical number of Au-NPs per p-NIPAM microgel particle could be calculated. For experiments with a low degree of loading the ratio of Au-NPs per microgel particle was kept constant at 241 for the different microgels. In contrast the ratio was 1133 for high loading experiments.

3.3.1 Low loading regime. In order to study the influence of the swelling state of the microgel on the optical properties of the entrapped Au-NPs, temperature dependent UV-Vis absorbance measurements were performed. The results are shown in Fig. 3 (left column).

The TEM images (Fig. 3, right column) show that the Au-NPs are more concentrated on the outside of the microgel particle for the p-NIPAM$_5$ and p-NIPAM$_{10}$ particles (Fig. 3b2 and c2) compared to p-NIPAM$_{0.25}$ particles (Fig. 3a2). Furthermore, image analysis reveals an average radius of the Au-NPs of 10.3 nm, which is in good agreement with the radius obtained for the bare gold nanoparticles prior to mixing with the microgels. We define the loading efficiency as the percentage of gold particles observed to be adsorbed to each gold particle compared to the nominal number added to the solution. As seen in Table 2, the loading efficiency is around 37% for all three p-NIPAM microgels. Taking the error of $\approx 10\%$ into account, the loading efficiency can be considered to be constant for the different cross-linker concentrations.
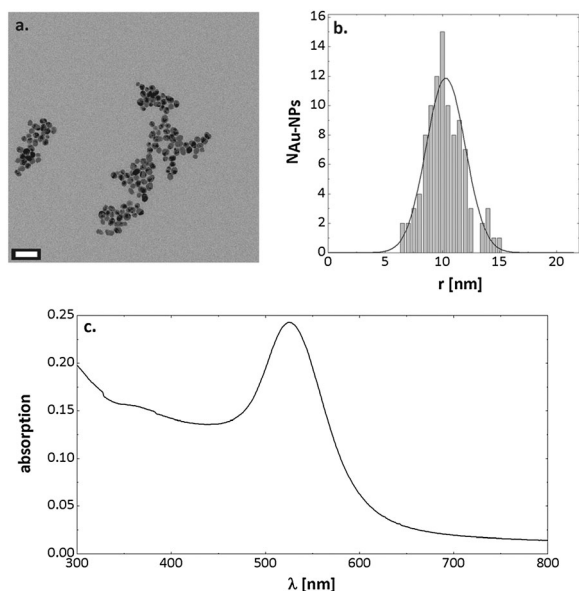
Fig. 2 TEM-image (scale bar: 80 nm) (a), size distribution (b) and UV-Vis spectrum (c) of synthesised Au-NPs.
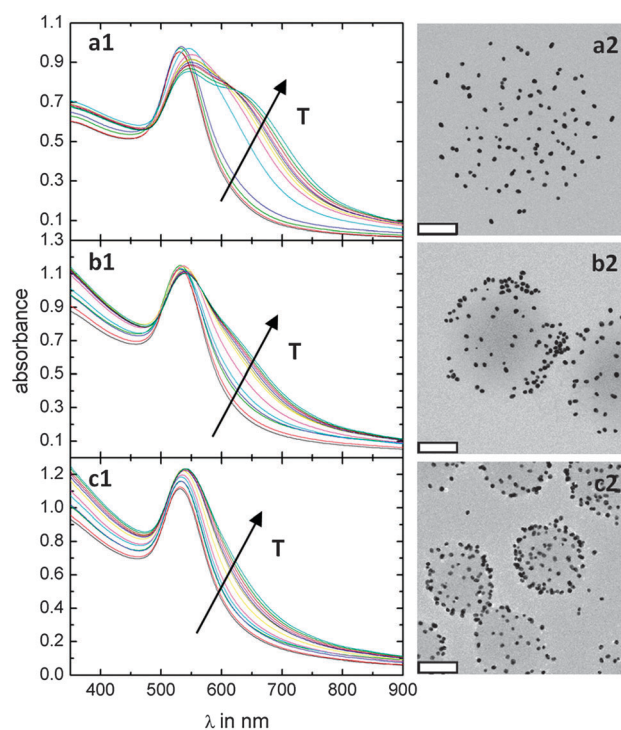

Fig. 3 TEM images (scale bar: 200 nm) and UV-Vis spectra of p-NIPAM$_{0.25}$ (a1 and a2), p-NIPAM$_5$ (b1 and b2) and p-NIPAM$_{10}$ (c1 and c2) for the low loading regime of Au-NPs.

15626 | *Phys. Chem. Chem. Phys.*, 2013, **15**, 15623–15631

This journal is © the Owner Societies 2013

Table 2 Loading efficiency for the low loading regime of Au-NPs

MBA [%]	$N_{Au,max}$	$N_{Au,adsorbed}$	$N_{Au,adsorbed}$ [%]
0.25	241	99	41
5	241	86	36
10	241	83	34

The difference in Au-NP loading and in plasmon coupling of the p-NIPAM$_{0.25}$ sample is of particular interest. Although the microgel particle is only barely visible by electron microscopy due to its very low contrast, the circular assembly of Au-NPs enables the microgel particle to be easily recognised in the images, and even allows the size to be estimated. UV-Vis spectra at different temperatures are presented in Fig. 3a1. Compared to the spectrum of bare Au-NPs (Fig. 2c), the absorption maximum is redshifted by ≈ 10 nm to 535 nm at low temperatures, where the p-NIPAM particles are in the swollen state. This redshift is attributed to the increase in the local refractive index environment in the presence of p-NIPAM chains. If spectra recorded at different temperatures are compared, two effects can be observed: (1) the plasmon resonance at 535 nm redshifts with increasing temperature, which is related to a further refractive index increase during the microgel collapse. (2) A shoulder appears at ≈ 675 nm when the temperature increases. This shoulder is related to plasmon coupling between Au-NPs. During the microgel collapse the distance between neighbouring Au-NPs decreases and plasmon resonance coupling can occur if this distance is small enough. Hence, the spectra at higher temperatures are a superposition of the spectra of isolated Au-NPs and aggregates of Au-NPs present in the microgel. Due to the rather low loading density these aggregates are assumed to be almost exclusively pairs of Au-NPs.

To further investigate the origin of the observed, strong plasmon resonance coupling at temperatures above the VPTT, SAXS measurements of all three loaded microgels were done at 20 °C and 50 °C. The measured scattering curves of Au loaded p-NIPAM$_{10}$ are presented in Fig. 4.
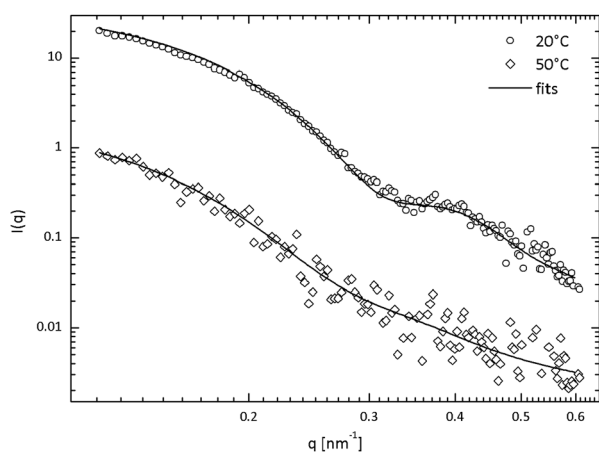
Fig. 4 Saxs-scattering curves and the corresponding fits of p-NIPAM$_{10}$ loaded with gold nanoparticles in the low loading regime at 20 °C and 50 °C.

Table 3 Radii, amounts of individual and pairs of Au-NPs and the ratio (ν) of the radius of the semi-principal axis to the radius of the equatorial axis obtained by SAXS-measurements for the low loading regime

| MBA [%]	T [°C]	R [nm]	x_{sphere} [%]	$x_{ellipsoid}$ [%]	ν
0.25	20	13.1	100	0	1
0.25	50	13.2	0	100	1.9
5	20	13.0	100	0	1
5	50	13.8	78	22	2.2
10	20	13.2	100	0	1
10	50	13.0	84	16	1.9

Due to the huge difference in the electron density of Au-NPs and the polymer–water-matrix, the X-ray scattering from Au dominates the signal, while the polymer particles and water contribute only weakly. Due to the long measurement time, a small amount of aggregation of the Au-NPs occurs, which leads to sedimentation and a decrease in the intensity signal above the VPTT. Assuming no contribution from the structure factor, the data can be well described using a form factor for polydisperse, homogeneous spheres below the VPTT ($T = 20$ °C). However, for temperatures above the VPPT, a simple polydisperse sphere form factor failed to describe the measured SAXS profiles. Instead we used a form factor corresponding to ellipsoids to fit the data, in order to account for gold particle dimers. Table 3 shows the calculated radii for the spheres and ellipsoids as well as the ratio of the radius of the semi-principal axis to the radius of the equatorial axis (ν) in the case of ellipsoids. It is evident that the value of ν corresponds closely to the expected one for dimers (≈ 2).

3.3.2 High loading regime. The results for hybrid samples in the high loading regime (1133 Au-NPs per p-NIPAM microgel particle) are shown in Fig. 5a1 and a2 for p-NIPAM$_{0.25}$, in Fig. 5b1 and b2 for p-NIPAM$_5$ and in Fig. 5c1 and c2 for p-NIPAM$_{10}$.

The TEM-images clearly reveal a substantially higher degree of Au-NP loading compared to the microgels with less initial Au-NP added, as expected. The loading efficiencies are presented in Table 4 and show a slight decrease compared to the low loading regime (Table 2). This might be an indication for saturated adsorption at high added loadings of Au-NPs but the effect is too weak for a strong statement.

For microgels with an MBA content of 5 mol% and 10 mol%, the Au-NPs are concentrated in the outer part of the polymer network. This local enhancement in particle numbers is more evident for the microgels with higher loadings. The UV-Vis spectra show that even for low temperatures all three loaded p-NIPAM microgel particles possess a shoulder at longer wavelengths than the plasmon resonance at ≈ 535 nm. For all three types of p-NIPAM particles there is an absorption band at ≈ 675 nm, which increases with increasing temperature, i.e., when the microgel shrinks. Furthermore, for p-NIPAM$_{0.25}$ a third shoulder at ≈ 750 nm appears in the UV-Vis spectrum at high temperatures.
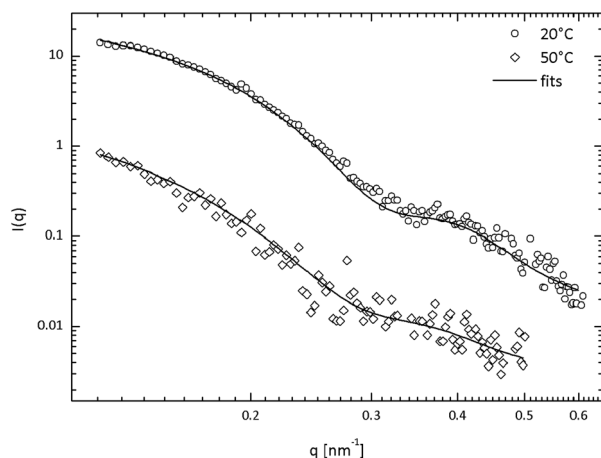
The scattering curves obtained from the SAXS measurements and the corresponding fits for Au loaded p-NIPAM$_{10}$ in the high loading regime are shown in Fig. 6.
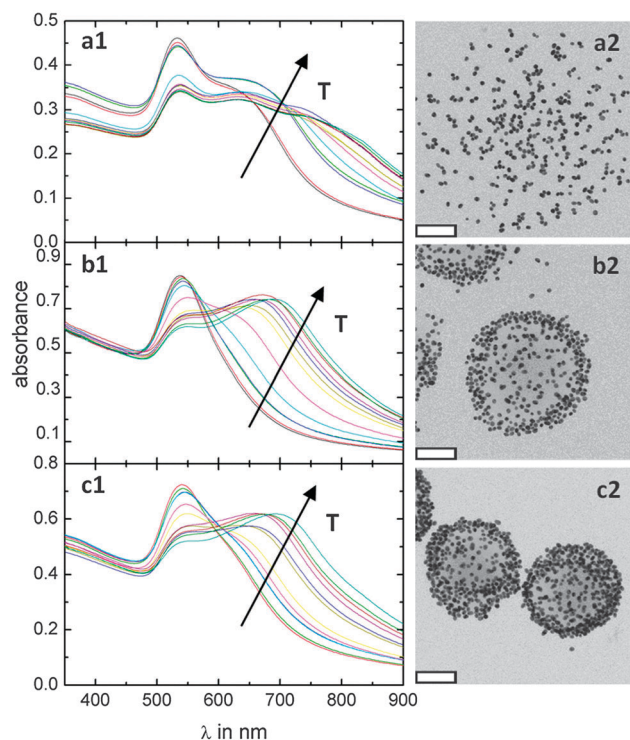
Fig. 5 TEM images (scale bar: 200 nm) and UV-Vis spectra of p-NIPAM$_{0.25}$ (a1 and a2), p-NIPAM$_5$ (b1 and b2) and p-NIPAM$_{10}$ (c1 and c2) for the high loading regime of Au-NPs.

Table 4 Loading efficiency for the high loading regime of Au-NPs

MBA [%]	$N_{Au,max}$	$N_{Au,adsorbed}$	$N_{Au,adsorbed}$ [%]
0.25	1133	359	32
5	1133	319	28
10	1133	337	30

Fig. 6 Scattering curves and the corresponding fits of p-NIPAM$_{10}$ loaded with gold nanoparticles in the high loading regime at 20 °C and 50 °C.

The data obtained from fitting of the SAXS-curves are presented in Table 5. Even for these higher loadings, the volume ratio remains rather small and structure factor contributions

Table 5 Radii, amounts of individual and pairs of Au-NPs and the ratio (ν) of the radius of the semi-principal axis to the radius of the equatorial axis obtained by SAXS-measurements for the high loading regime

| MBA [%]	T [°C]	R [nm]	x_{sphere} [%]	$x_{ellipsoid}$ [%]	ν
0.25	20	13.9	0	100	2.4
0.25	50	12.7	0	100	2.2
5	20	12.8	87	13	1.9
5	50	13.2	0	100	1.9
10	20	13.2	80	20	1.9
10	50	13.5	0	100	1.9

could be neglected. For all three microgel particles and both temperatures, some of the Au-NPs are present as ellipsoids, indicating the formation of Au-NP dimers.

4 Discussion

The results presented here demonstrate that there is a high affinity of citrate stabilised Au-NPs for p-NIPAM microgels, despite the fact that both the gold particles and the gel particles are negatively charged. This affinity may be attributed to attractive interactions between the nanoparticles and the acrylamide moieties of the p-NIPAM, as amines are known to chemisorb strongly to gold metal surfaces.

The presence of the gold particles strongly affects the swelling behaviour of the p-NIPAM. This can be demonstrated most easily by dynamic light scattering (DLS), as shown in Fig. 7. A decrease in the hydrodynamic radius of the polymer particles is observed, particularly for microgels in the swollen state, *i.e.*, at temperatures below the volume phase transition temperature (VPTT) of the microgels. The gold particles cause some partial contraction of the polymer network, when they become embedded; this is likely to be due to polymer conformation changes to facilitate amide adsorption to the gold surfaces.

In addition, we performed angle-dependent DLS measurements for pure microgels and the hybrid samples and the results are shown in Fig. S3 (ESI†). A strong, linear correlation between the determined decay rates (Γ) and the square of the scattering vector (Q) is observed for all samples. This proves that purely translational diffusion is probed and consequently the Stokes–Einstein equation may be used to determine the hydrodynamic radii from the mean values of Γ. From the slope of the linear fit the hydrodynamic radii were calculated and are in good agreement with the results at a fixed angle of 60°. For the highest crosslinked sample (p-NIPAM$_{10}$), no change occurs below the VPTT.
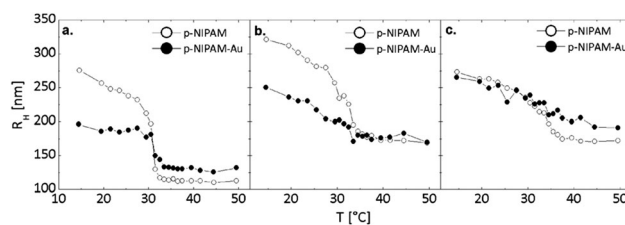
Fig. 7 Swelling curves of pure p-NIPAM$_{0.25}$ (a), p-NIPAM$_5$ (b) and p-NIPAM$_{10}$ (c) compared to swelling curves after loading with Au-NPs.

15628 | *Phys. Chem. Chem. Phys.*, 2013, **15**, 15623–15631

This journal is © the Owner Societies 2013

The Au-NP immobilization was performed at room temperatures and hence far below the VPTTs. The low and medium cross-linked microgels are rather elastic and flexible and consequently network deformation is already observed in the swollen state. The sample with the highest cross-linker density is less flexible and therefore the loading of Au-NPs has a minor effect. Burmistrova *et al.* showed by Atomic Force Microscope indentation measurements that the elastic modulus increases with increasing amounts of cross-linker.[32] The Au-NPs partially hinder the microgel collapse at the VPTT which leads to a slight increase in the microgel volume in comparison to the unloaded polymer particles.

The dimensions of the p-NIPAM$_{0.25}$ particles obtained from TEM images (Fig. 3a2 and 5a2) differ considerably from the values obtained by DLS (Fig. 7). The TEM images indicate a diameter of more than 1 μm while DLS measurements yield a maximum diameter of about 550 nm. We explain this difference in terms of the sample preparation for the TEM analysis. The TEM samples were prepared by drop-casting a highly dilute, aqueous dispersion onto carbon-coated copper grids, and in this case, adhesion forces between the carbon film and the microgel particles induce a strong flattening and stretching of the particles. This effect can also be observed for block copolymer micelles with a very soft corona. Nevertheless, the TEM images clearly demonstrate the important influence of cross-linker density on the deposition of gold particles within the polymer shell. Consequently, the particle dimensions are most easily determined by ensemble DLS measurements, which avoid the morphology changes induced by TEM sample preparation.

The localised surface plasmon resonance of the Au-NPs adsorbed to the microgels (535 nm) is redshifted compared to the peak wavelength found for bare Au-NPs in aqueous dispersion (525 nm). Incorporation of the Au-NPs into the polymer networks increases the refractive index in the vicinity of the Au-NPs. It is well-known that an increase in refractive index leads to a shift of the plasmon resonance towards higher wavelengths. The observed shift of ≈10 nm indicates a strong interaction between the Au-NPs and the polymer network of the microgels.[20]
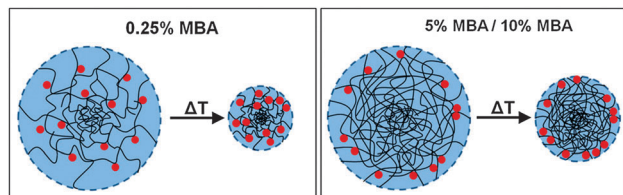
In addition to this red-shift, a second absorption band appears at higher wavelengths (around 675 nm). The intensity of this peak or shoulder strongly depends on the loading density. In case of the low loading regime, the shoulder only appears at high temperatures. In the higher loading regime, the shoulder already appears in the fully swollen state of the microgels at room temperature. The appearance of this absorption band at higher wavelengths can be explained by surface plasmon resonance coupling between individual Au-NPs. If the distance between individual Au-NPs is below ≈5 nm, dipolar coupling shifts the resonance to higher wavelengths. During the volume phase transition of p-NIPAM the distance between the adsorbed Au-NPs decreases. This effect is more pronounced for p-NIPAM$_{0.25}$ (Fig. 3a1 and 5a1) due to its much smaller value of α. In other words the relative volume change induced by temperature is much more pronounced for this microgel compared to the higher cross-linked microgels. For the highly loaded p-NIPAM$_{0.25}$ microgels the distance between adsorbed Au-NPs is already small enough at room temperature (swollen state) so that plasmon coupling is observed (Fig. 5a1). With increasing temperature a second shoulder appears at around 750 nm which indicates the formation of even larger resonantly coupled Au-NPs.

The results obtained using UV-Vis spectroscopy are validated by SAXS measurements below and above the VPTT. In the low loading regime at 20 °C the scattering curves for all three microgel systems can be described using form factors for polydisperse, homogeneous spheres representing individual, non-interacting Au-NPs with a radius of ≈13 nm (Table 3). This is in good agreement with the UV-Vis spectra below the VPTT (Fig. 3) where no plasmon coupling is evident. An increase in temperature above the VPTT leads to the formation of Au-NP pairs which can be considered as objects with a more ellipsoidal shape with an aspect ratio, $\nu \approx 2$. In accordance with the corresponding UV-Vis spectra, the SAXS curve of p-NIPAM$_{0.25}$ can be described by the presence of ellipsoids ($\nu = 1.9$) whereas the higher cross-linked p-NIPAM microgels are loaded with a mixture of Au-NP spheres and Au-NP pairs. This is supported by a less pronounced shoulder at a wavelength of ≈675 nm in the UV-Vis spectra.

The same investigations were done for the high loading regime, where only ellipsoids ($\nu \approx 2$) are present in p-NIPAM$_{0.25}$ below and above the VPTT. The scattering curves for p-NIPAM$_5$ and p-NIPAM$_{10}$ are well fitted by contributions from a mixture of spheres and ellipsoids ($\nu \approx 2$) at 20 °C and just ellipsoids ($\nu = 1.9$) at 50 °C (Table 5). These results are also in good agreement with the corresponding UV-Vis spectra (Fig. 5). The determined radii for spheres and ellipsoids are ≈13 nm which is in the same range as determined for pure Au-NPs.

To obtain more detailed information about the distribution of the Au-NPs within the polymer network, TEM images were recorded (Fig. 3a2, b2, c2 and 5a2, b2, c2). The measured images for the Au-NP loaded p-NIPAM$_5$ and p-NIPAM$_{10}$ clearly demonstrate that increasing amounts of added Au-NPs lead to a higher density of Au-NPs in the polymer network. However, for 5 mol% and 10 mol% cross-linker, the images show that the Au-NPs seem to be located in the outer shell of the microgel network. This suggests that transport of the gold particles into the core of the microgels is hindered by densely cross linked pores. Access to the centre of the microgels is controlled by the cross-linker density, which determines the mesh size distribution within the microgel particles. In contrast, the TEM images of p-NIPAM$_{0.25}$ show that the Au-NPs are distributed throughout the microgel particles for both loading regimes. It is expected that the microgel particles will possess a rather pronounced radial gradient of cross-links due to the different reaction kinetics of the cross-linker MBA and the monomer NIPAM. Hence, p-NIPAM microgels consist of an inhomogeneous network structure with a gradient in mesh sizes.[33] Increasing the MBA content leads to a larger region of the particle within which the polymer network is highly cross-linked. Therefore, p-NIPAM$_{0.25}$ consists of a small highly crosslinked core and a larger, outer region where the network is more open. Hence, the Au-NPs are able to diffuse

This journal is © the Owner Societies 2013

Phys. Chem. Chem. Phys., 2013, **15**, 15623–15631 | **15629**

Fig. 8 Diagram illustrating the effects of cross-linker concentration on the distribution of gold particles in the microgels during collapse.

deeper inside the microgel particles than in the case of p-NIPAM$_5$ and p-NIPAM$_{10}$ which is demonstrated in Fig. 8. Therefore, the penetration depth of the Au-NPs depends on the cross-linker concentration.

As shown in the results, the Au-NPs are strongly adsorbed to the microgel particles. During the mixing process the citrate stabilised Au-NPs are able to diffuse rather freely in and out of the polymer network but the maximum penetration depth is limited by the mesh size. Therefore, the mesh size in the outer regions is not less than 20 nm since the Au-NPs can be loaded within the polymer network. The region with meshes larger than 20 nm increases with decreasing cross-linker content, leading to a deeper penetration depth of the Au-NPs. After centrifugation most of the citrate stabiliser is removed from the Au-NPs and due to the strong affinity for the amide groups on the polymer they are mainly stabilised by the surrounding polymer segments (Fig. 1). This can clearly be seen in the TEM, where the Au-free areas around the loaded microgels demonstrate that no leakage of the gold particles out of the microgels occurs. An increase in temperature above the VPTT leads to a partial aggregation of the metastable Au-NPs, which is more pronounced for microgels with a low content of MBA, probably due to the higher mobility of the NPs. In the case of 5 mol% and 10 mol% MBA, plasmon coupling between the Au particles is evident due to the strong accumulation of the Au-NPs in the outer shell of the microgels. Surprisingly for the 0.25 mol% cross-linked sample we also observe strong plasmon resonance coupling, although the Au-NP distribution appears rather homogeneous from TEM analysis. The distance between individual Au-NPs entrapped in the p-NIPAM$_{0.25}$ is too large for significant plasmon coupling to occur.

Table 6 shows the interparticle spacing of the swollen and collapsed p-NIPAM$_{0.25}$ assuming the nanoparticles are homogeneously distributed within the polymer network. The interparticle spacing is much larger than the particle diameters and plasmon resonance coupling should not be evident, even in the fully collapsed state. Cryo-TEM images of the p-NIPAM microgels in the high loading regime are shown in the ESI† (Fig. S4). The image of p-NIPAM$_{0.25}$ indicates that the Au-NPs are located

preferentially in the outer region of the polymer network. In the case of p-NIPAM$_5$ and p-NIPAM$_{10}$ it is even clearer to see that the NPs are located within a rather thin shell in the outer part of the microgels.

5 Conclusions

The effect of cross-linker density of poly-N-isopropylacrylamide (p-NIPAM) microgels on loading with spherical gold nanoparticles (average radius from TEM: 10.3 nm) has been investigated. By mixing dilute microgel dispersions with different amounts of citrate-stabilised Au-NPs, hybrid microgel systems with different gold contents and different optical properties can be achieved. The loading efficiency decreases slightly with increasing concentrations of added Au-NPs. Analysis using transmission electron microscopy supports the assumption of an inhomogeneous network structure of the microgel colloids with a dense core and a more open shell. The volume of the denser core region increases with increasing cross-linker content leading to reduced penetration depths of the Au-NPs. Thus the volume of the less cross-linked shell with mesh sizes >20.5 nm decreases limiting the Au-NP distribution to the outer microgel regions where the mesh size is larger than the Au-NP dimensions. The optical properties of the hybrid particles were studied using UV-Vis spectroscopy. Temperature dependent measurements revealed strong plasmon resonance coupling as the microgels shrink at the VPTT. Coupling increases with increasing nanoparticle loading but decreases with increasing microgel network connectivity. This allows the preparation of hybrid systems, which demonstrate controlled plasmon resonance coupling. For example, for low gold particle loadings and highly cross-linked microgels, only weak coupling is found. In contrast for high loading densities and low cross-linker densities, strong coupling is observed. The plasmon resonance coupling in our hybrid microgels is due to the formation of nanoparticle dimers. This dimer formation in thermoresponsive microgels has been demonstrated here for the first time and verified by SAXS measurements.

The results from our investigations show that the cross-linker density can be used as a convenient parameter to control the morphology of inorganic–organic hybrid microgels containing plasmonic gold nanoparticles.

Acknowledgements

Table 6 Average distance of Au-NPs within the microgel network for p-NIPAM$_{0.25}$ assuming a homogeneous distribution over the entire microgel

$N_{Au,adsorbed}$	d_{298K} [nm]	d_{323K} [nm]
99	103	49
359	67	32

References

1 R. Pelton, *Adv. Colloid Interface Sci.*, 2000, **85**, 1–33.

2 H. Senff and W. Richtering, *J. Chem. Phys.*, 1999, **111**, 1705–1711.

3 K. Kratz, T. Hellweg and W. Eimer, *Polymer*, 2001, **42**, 6631–6639.

4 I. Berndt and W. Richtering, *Macromolecules*, 2003, **36**, 8780–8785.

5 M. Stieger, J. S. Pedersen, P. Lindner and W. Richtering, *Langmuir*, 2004, **20**, 7283–7292.

6 A. Fernández-Nieves, A. Fernández-Barbero, B. Vincent and F. de las Nieves, *Macromolecules*, 2000, **33**, 2114–2118.

7 K. Kratz, T. Hellweg and W. Eimer, *Colloids Surf., A*, 2000, **170**, 137–149.

8 T. Hoare and R. Pelton, *Macromolecules*, 2004, **37**, 2544–2550.

9 M. Shibayama, F. Ikkai, S. Inamoto, S. Nomura and C. C. Han, *J. Chem. Phys.*, 1996, **105**, 4358–4366.

10 M. Karg, I. Pastoriza-Santos, B. Rodriguez-Gonzlez, R. von Klitzing, S. Wellert and T. Hellweg, *Langmuir*, 2008, **24**, 6300–6306.

11 M. Karg and T. Hellweg, *J. Mater. Chem.*, 2009, **19**, 8714–8727.

12 M. Agrawal, S. Gupta and M. Stamm, *J. Mater. Chem.*, 2011, **21**, 615–627.

13 M. Das, H. Zhang and E. Kumacheva, *Annu. Rev. Mater. Res.*, 2006, **36**, 117–142.

14 A. Z. Pich and H.-J. P. Adler, *Polym. Int.*, 2007, **56**, 291–307.

15 R. Contreras-Cáceres, A. Sanchez-Iglesias, M. Karg, I. P.-S. J. Pérez-Juste, J. Pacifico, T. Hellweg, A. Fernández-Barbero and L. M. Liz-Marzán, *Adv. Mater.*, 2009, **20**, 1666–1670.

16 M. Karg, I. Pastoriza-Santos, L. M. Liz-Marzán and T. Hellweg, *ChemPhysChem*, 2006, **7**, 2298–2301.

17 M. Karg, S. Jaber, T. Hellweg and P. Mulvaney, *Langmuir*, 2011, **27**, 820–827.

18 A. Pich, A. Karak, Y. Lu, A. K. Ghosh and H.-J. P. Adler, *Macromol. Rapid Commun.*, 2006, **27**, 344–350.

19 Y. Lu, S. Proch, M. Schrinner, M. Drechsler, R. Kempe and M. Ballauff, *J. Mater. Chem.*, 2009, **19**, 3955–3961.

20 H. Lange, B. H. Juarez, A. Carl, M. Richter, N. G. Bastus, H. Weller, C. Thomsen, R. von Klitzing and A. Knorr, *Langmuir*, 2012, **24**, 8862–8866.

21 C. Jones and L. Lyon, *J. Am. Chem. Soc.*, 2003, **125**, 460–465.

22 C. Jones, M. Serpe, L. Schroeder and L. Lyon, *J. Am. Chem. Soc.*, 2003, **125**, 5292–5293.

23 M. Das, N. Sanson, D. Fava and E. Kumacheva, *Langmuir*, 2007, **23**, 196–201.

24 M. Karg, I. Pastoriza-Santos, J. Pérez-Juste, T. Hellweg and L. Liz-Marzán, *Small*, 2007, **3**, 1222–1229.

25 M. Karg, Y. Lu, E. Carb-Argibay, I. Pastoriza-Santos, J. Prez-Juste, L. M. Liz-Marzn and T. Hellweg, *Langmuir*, 2009, **25**, 3163–3167.

26 R. Pelton and P. Chibante, *Colloids Surf.*, 1986, **20**, 247–256.

27 B. V. Enüstün and J. Turkevich, *J. Am. Chem. Soc.*, 1963, **85**, 3317–3328.

28 S. W. Provencher, *Comput. Phys. Commun.*, 1982, **27**, 213–227.

29 K. Kratz and W. Eimer, *Ber. Bunsen-Ges.*, 1998, **102**, 848–853.

30 K. Kratz, T. Hellweg and W. Eimer, *Polymer*, 2001, **42**, 6631–6639.

31 J. Gao and Z. Hu, *Langmuir*, 2002, **18**, 1360.

32 A. Burmistrova, M. Richter, C. Uzum and R. v. Klitzing, *Colloid Polym. Sci.*, 2011, **289**, 613–624.

33 M. Stieger, J. S. Pedersen, P. Lindner and W. Richtering, *Langmuir*, 2004, **20**, 7283–7292.

This journal is © the Owner Societies 2013

Phys. Chem. Chem. Phys., 2013, **15**, 15623–15631 | **15631**